Rayleigh–wave multicomponent crosscorrelation–based source strength distribution inversion. Part 1: Theory and numerical examples

SCHOLARONE™
Manuscripts

submitted to *Geophys. J. Int.*

Rayleigh-wave multicomponent crosscorrelation-based source strength distribution inversion. Part 1: Theory and numerical examples

Zongbo Xu[1], T. Dylan Mikesell[1], Gabriel Gribler[1], and Aurélien Mordret[2]

[1]*Environmental Seismology Laboratory, Department of Geosciences,*

Boise State University, Boise, ID, USA.

[2]*Department of Earth, Atmospheric, and Planetary Sciences,*

Massachusetts Institute of Technology, Cambridge, MA, USA.

SUMMARY

People commonly use cross-correlation based seismic interferometry to retrieve Green's functions from ambient seismic noise recordings. This approach requires that seismic sources are isotropically distributed in all directions around two receivers. However, this assumption is rarely valid in practice. Thus people have begun to apply full-waveform inversion theory to seismic noise crosscorrelation functions, functions that include both source and structure information. Source information (like locations and strengths) are essential for accurate structure information estimation. In this paper, we explain physically two types of source sensitivity kernels: one derived from traveltime misfits and the other derived from waveform misfits. We use these kernels for source inversion, and demonstrate the benefits of using multicomponent crosscorrelations in this source estimation process.

2   *Xu et al.*

1   INTRODUCTION

People nowadays commonly crosscorrelate ambient seismic recordings of two sensors to retrieve the surface-wave Green's functions between the two sensors (e.g. Snieder 2004). Assuming the crosscorrelation function is the band-limited Green's functions, one can estimate subsurface geologic structures (e.g. Shapiro et al. 2005). The crosscorrelation method, or seismic interferometry, requires that seismic sources are isotropically distributed in all directions around two receivers (e.g. Wapenaar & Fokkema 2006). However, this assumption is rarely valid in practice. An anisotropic source distribution will bias the retrieved Green's functions and the resulting subsurface geologic inferences (e.g. Yang & Ritzwoller 2008; Yao & van Der Hilst 2009). To reduce this bias, people have developed many approaches to compensate for the anisotropic source distribution. For example, people use beamforming (e.g. Rost & Thomas 2002) to estimate the seismic source direction and then use this direction to correct the retrieved Green's function or surface-wave dispersion estimates (e.g. Nakata et al. 2015; Cheng et al. 2016). When using beamforming, one assumes that the underground is isotropic and laterally homogeneous. This assumption for the subsurface structures is also not always valid. For anisotropic seismic source distributions and laterally heterogeneous subsurface structures, people have proposed not to use the seismic crosscorrelations to approximate Green's functions, but instead apply full-waveform inversion theory to the seismic crosscorrelations (Tromp et al. 2010; Fichtner 2015). The seismic crosscorrelations include both source distribution and subsurface structure information. If one wants to estimate the subsurface structure, one has to first (e.g. Nakata et al. 2015; Cheng et al. 2016), or simultaneously (e.g. Yao & van Der Hilst 2009; Harmon et al. 2010), unravel the anisotropic source information.

Seismic source distribution estimations is also relevant to studies of ambient seismic sources. For example, high-frequency (>1 Hz) ambient seismic noise can help people monitor underground hydrothermal acoustic sources (e.g. Cros et al. 2011) and microseismic sources at the exploration scale (e.g. Corciulo et al. 2012); 5-20 s period ambient seismic noise can be used to study the primary and secondary microseisms (e.g. Tian & Ritzwoller 2015; Juretzek & Hadziioannou 2016); 100 s period can be used to study the Earth hum (e.g. Rhie & Romanowicz 2006; Traer & Gerstoft 2014; Ardhuin et al. 2015).

People mainly locate seismic sources using two methods, an adjoint method and an adjoint-based inversion method. When using the adjoint method, people apply time reversal to recorded seismic waveforms and then find the location where the reversed waveforms are most similar to each other. This method includes backprojection (e.g. Ishii et al. 2005), reverse-time migration (e.g. Artman et al. 2010) and matched-field processing (e.g. Cros et al.

2011). These approaches do not involve so-called inversion compared to the adjoint-based inversion method. The adjoint-based inversion method combines time reversal and iterative optimization (e.g. Liu et al. 2004). When using either of these two methods, one assumes that the subsurface structure is known and then solve for the source parameters (e.g. location or moment tensors).

Rayleigh waves dominate ambient seismic noise. Multicomponent Rayleigh-wave data can bring benefits for estimating both source distributions and subsurface structure. The important multicomponent data for Rayleigh waves are the vertical (Z) and radial (R) components, where the R direction is parallel to a line or great-circle path between two sensors. If we assume vertical-force seismic sources, the $Z-Z$ component crosscorrelation (C_{ZZ}) is sensitive to the seismic sources in all directions, while the $R-R$ component crosscorrelation (C_{RR}) is more sensitive to in-line seismic sources than out-of-line sources (e.g. Haney et al. 2012; Xu & Mikesell 2017). Multicomponent data can also help to characterize Rayleigh waves more accurately than only the Z component data (e.g. Boaga et al. 2013; Gribler et al. 2016) and constrain the shear-wave velocity inversions (e.g. Arai & Tokimatsu 2004). Thus we study multicomponent crosscorrelations in the context of ambient noise full-waveform inversion in this paper.

We focus on multicomponent crosscorrelation source inversion in this paper. We adopt full-waveform inversion theory to estimate seismic source distributions. We compare the use of traveltime vs waveform information in inversion, and discuss the source sensitivity kernels for C_{ZZ} and C_{RR}. We present the whole inversion scheme in Section 2. In Section 3, we present the kernels for a single frequency and a frequency band, and we explain the physics behind these kernels. We then apply the multicomponent source kernels in three synthetic data examples and estimate the source distributions (Section 4). Finally, we discuss factors that affect the accuracy of the inversions in Section 5.

2 CROSSCORRELATION INVERSION SCHEME

We use full-waveform inversion theory to estimate seismic source distributions. In an inversion process, we define a misfit function to measure the difference between the synthetic and observed data (Section 2.1). The observed data in this paper are observed Rayleigh-wave crosscorrelations. We compute synthetic crosscorrelations using a forward modelling process based on the source model parameters, i.e. the source strength distribution (Section 2.2). We then update the source model parameters with an inversion method that minimizes the misfit

4 *Xu et al.*

function (Section 2.4). This is a common strategy in non-linear inverse problems (e.g. Aster et al. 2011)

2.1 Misfit functions

People define the misfit function (χ) based on physical properties of waveforms, for example traveltimes (e.g. Luo & Schuster 1991; Dahlen et al. 2000), envelopes (e.g. Fichtner et al. 2008; Bozdağ et al. 2011) or raw waveforms(e.g. Tromp et al. 2005). Here we use two misfit functions: the Rayleigh-wave waveform crosscorrelation (Equation 1) and wave traveltime (Equation 2). We define the waveform misfit function as

$$\chi = \frac{1}{2} \sum_{mn} \sum_{r_A r_B} \int [w(t)(C_{mn}(r_A, r_B, t) - C_{mn}^o(r_A, r_B, t))]^2 dt \tag{1}$$

where $w(t)$ is a time window, and $C_{mn}(r_A, r_B, t)$ and C_{mn}^o are the synthetic and observed crosscorrelations, respectively. The crosscorrelations are between sensor r_A and r_B; m, n represent the components, vertical (Z) or radial (R), from each of the two sensors, respectively. We use the time window to focus on certain parts of the observed crosscorrelations (e.g. Maggi et al. 2009; Fichtner et al. 2017). We define the traveltime misfit function following Luo & Schuster (1991) as

$$\chi = \frac{1}{2} \sum_{mn} \sum_{r_A r_B} (T_{syn}(r_A, r_B) - T_{obs}(r_A, r_B))^2, \tag{2}$$

where T_{syn} and T_{obs} represents the traveltime of the main Rayleigh-wave waveform in the synthetic and observed crosscorrelations, respectively. Luo & Schuster (1991) and Dahlen et al. (2000) describe how to measure the traveltime difference, $T_{syn} - T_{obs}$. We restate this measurement procedure in Appendix A. In this paper, we call the source inversions using the waveform and the traveltime misfit functions as the waveform inversion and the traveltime inversion, respectively.

2.2 Forward modelling process

We need synthetic data to calculate the misfit function. We compute synthetic crosscorrelations from a source distribution with the forward modelling process. People have discussed the whole forward modelling process explicitly (e.g. Wapenaar & Fokkema 2006; Tromp et al. 2010; Fichtner et al. 2017). We here review the main steps in the forward modelling process implemented in the frequency domain. We first write the seismic record at one sensor (r_A)

due to many sources as

$$U_{mp}(r_A, \omega) = \int_V G_{mp}(r_A, r_s, \omega) F_p(r_s, \omega) dr_s, \tag{3}$$

where $G_{mp}(r_A, r_s, \omega)$ is the Green's function representing the mth component displacement response at location r_A due to a point force in the p direction at the source position r_s, ω is the angular frequency, and $F_p(r_s, \omega)$ is the the source wavelet spectrum. We then crosscorrelate two sensor (r_A and r_B) records as

$$C_{mn}(r_A, r_B, \omega) = U_{mp}(r_A, \omega) U_{np}^*(r_B, \omega)$$

$$= \int_V G_{mp}(r_A, r_s, \omega) G_{np}^*(r_B, r_s, \omega) S_p(r_s, \omega) dr_s, \tag{4}$$

where the asterisk represents complex conjugation. Here we assume that all seismic sources are independent, thus

$$S_p(r_s, \omega) = F_p(r_s, \omega) F_p^*(r_s, \omega). \tag{5}$$

94 We note that the source strength, S_p, should be nonnegative for all frequencies.

The forward modelling process is computationally expensive. Equation 4 requires one simulation for one point force source at r_s in the p direction. If we have many seismic sources like traffic, we have to conduct many simulations. Therefore people have proposed to decrease the computation by using wavefield reciprocity (e.g. Tromp et al. 2010; Ermert et al. 2017). With the reciprocity (e.g. Aki & Richards 2002),

$$G_{mp}(r_A, r_s) = G_{pm}(r_s, r_A), \tag{6}$$

95 and we can modify the forward simulations by activating seismic sources at sensors (r_A),
96 instead of at real seismic sources (r_s). The number of sensors is normally less than the num-
97 ber of potential seismic sources in the source grid. This decreases the forward computation
98 dramatically.

99 2.3 Fréchet derivative with respect to source strength

Source inversion requires the Fréchet derivative of the misfit function due to perturbations in the source distribution (e.g. Fichtner 2015; Sager et al. 2018). Here we review the steps to derive the Fréchet derivative. First, we write the perturbation of the misfit function due to a perturbation in the synthetic crosscorrelation as (e.g. Fichtner 2015)

$$\delta\chi(r_A, r_B) = \int_\omega \delta C_{mn}(r_A, r_B, \omega) f d\omega, \tag{7}$$

6   *Xu et al.*

where f is the adjoint source. The adjoint source is derived from the misfit function, and we show how we derive the traveltime and waveform adjoint sources in Appendices A and B.

We then write the perturbation of the synthetic crosscorrelation (Equation 4) with a first-order term as

$$\delta C_{mn}(r_A, r_B, \omega) \approx \int_V G_{mp}(r_A, r_s, \omega) G_{np}^*(r_B, r_s, \omega) \delta S_p(r_s, \omega) dr_s$$
$$+ \int_V \delta[G_{mp}(r_A, r_s, \omega) G_{np}^*(r_B, r_s, \omega)] S_p(r_s, \omega) dr_s, \tag{8}$$

where the first part in the right hand side is for perturbations in the source, and the second part is for perturbations in the Green's functions. These two parts provide Fréchet source and structure derivatives (Fichtner 2015). We focus on the source derivative in this paper; thus we assume that the subsurface structure and the Green's functions are known. This assumption is common in source studies (e.g. Liu et al. 2004; Ishii et al. 2005; Artman et al. 2010). We rewrite the perturbation of the crosscorrelation with respect to source strength perturbations as

$$\delta C_{mn}(r_A, r_B, \omega) \approx \int_V G_{mp}(r_A, r_s, \omega) G_{np}^*(r_B, r_s, \omega) \delta S_p(r_s, \omega) dr_s. \tag{9}$$

We write the Fréchet derivative of the misfit function due to perturbations in the source strength by combining Equations 7 and 9 as

$$\delta\chi(r_A, r_B) = \int_\omega \int_V G_{mp}(r_A, r_s, \omega) G_{np}^*(r_B, r_s, \omega) \delta S_p(r_s, \omega) f dr_s d\omega, \tag{10}$$
$$= \int_\omega \int_V K_{mn}(r_A, r_B, \omega) \delta S_p(r_s, \omega) dr_s d\omega, \tag{11}$$

where

$$K_{mn}(r_A, r_B, \omega) = G_{mp}(r_A, r_s, \omega) G_{np}^*(r_B, r_s, \omega) f. \tag{12}$$

K_{mn} is called the source kernel (e.g. Fichtner et al. 2017). The kernel indicates the sensitivity of the misfit function to the source strength at r_s, $S_p(r_s, \omega)$. In practice, people assume that the spectral shapes for all sources (S_p) are similar (e.g. Ermert et al. 2017). Thus we assume that $S_p^0 N = S_p$, where S_p^0 is the assumed source spectrum and N is a ratio. N is always positive due to Equation 5. Finally, we rewrite Equations 11 and 12 as

$$\delta\chi(r_A, r_B) = \int_\omega \int_V K_{mn}(r_A, r_B, \omega) \delta N(r_s) dr_s d\omega \tag{13}$$

and

$$K_{mn}(r_A, r_B, \omega) = G_{mp}(r_A, r_s, \omega) G_{np}^*(r_B, r_s, \omega) S_p^0 f \tag{14}$$
$$= [G_{mp}(r_A, r_s, \omega) F_p^0][G_{np}(r_B, r_s, \omega) F_p^0]^* f, \tag{15}$$

102 where $S_p^0 = F_p^0(F_p^0)^*$. Equation 15 is convenient to use because we can easily compute synthetic

103 seismic recordings $(G_{mp}F_p^0)$ with the same numerical simulations used to create synthetic

104 crosscorrelation functions. Thus in the following context, we use $N(r_s)$ as the source strength

105 distribution model and use Equation 15 to calculate source sensitivity kernels.

106 ## 2.4 Inversion strategy

107 We use a gradient-decent strategy (e.g. Ermert et al. 2017), which is an iterative method. The

108 traveltime misfit function (Equation 2) is obviously a non-linear problem, while the waveform

109 misfit function (Equation 1) can be viewed as a linear problem. However, the waveform misfit

110 function is too large to be solved with linear inversion methods and iterative methods are a

111 better option on such large problems for the sake of memory (e.g. Aster et al. 2011). Thus we

112 solve the waveform misfit function with the iterative method as well. Another way to address

113 this problem is using the adjoint operator (e.g. Thorson & Claerbout 1985), for example, the

114 matched-field processing method (e.g. Cros et al. 2011; Corciulo et al. 2012) and microseismic

115 reverse-time migration (e.g. Artman et al. 2010). We discuss the link between the waveform

116 inversion and the matched-field processing and reverse-time migration methods in Appendix

117 C.

In the waveform inversion, we sum the kernels among all sensor pairs in a frequency band $[\omega_1, \omega_2]$ as

$$K = \sum_{mn} \sum_{r_A r_B} \int_{\omega_1}^{\omega_2} K_{mn}(r_A, r_B, \omega) d\omega. \tag{16}$$

If we only use vertical data, K is a summed K_{ZZ} among all sensor pairs; if we use both C_{ZZ} and C_{RR}, $K = K_{ZZ} + K_{RR}$ among all sensor pairs. We then multiply the summed kernel (K) with a step size (p) to update the source distribution in the ith iteration as

$$N_{i+1}(r_s) = N_i(r_s) - pK. \tag{17}$$

However, if we subtract the product (pK) directly, negative source strength values may appear. The negative source strength is not physical because of Equation 5. Thus we need to make sure that the updated source strengths are all nonnegative. We apply a positivity constraint (Johansen 1977) to the inversion such that Equation 13 becomes

$$\delta\chi(r_A, r_B) = \sum_{mn} \sum_{r_A r_B} \int_\omega \int_V K_{mn}(r_A, r_B, \omega) N(r_s) \delta ln[N(r_s)] dr_s d\omega \tag{18}$$

where ln is the natural logarithm. We then update the source strength distribution as

$$N_{i+1}(r_s) = N_i(r_s) e^{-pN_i(r_s)K}, \tag{19}$$

8 *Xu et al.*

¹¹⁸ where the exponential term is always positive. We note that if set our initial source strength

¹¹⁹ as nonnegative, the updated strengths will be nonnegative.

¹²⁰ We choose the step size (p) from many potential step size values. We update the source

¹²¹ strength distribution (N_i) using Equation 19 and the potential step sizes (e.g. $p = 10^{-6}, 10^{-5}, ...10^{-1}$).

¹²² For each step size, we have an updated source distribution model (N_{i+1}), and we compute

¹²³ synthetic crosscorrelations using Equation 4. We then calculate the corresponding misfit func-

¹²⁴ tion. Among these misfit values, we choose the step size that gives the minimum misfit. If the

¹²⁵ minimum misfit is less than an update criteria (C_u), we adopt the step size and update the

¹²⁶ source model; if not, we do not update this iteration and instead expand the frequency band.

¹²⁷ Details about the inversion are presented in Section 4.

3 RAYLEIGH-WAVE SOURCE KERNELS

¹²⁹ We present and describe the source kernels for Rayleigh waves of multicomponent crosscor-

¹³⁰ relations (C_{ZZ} and C_{RR}). In calculating the kernels, we require synthetic seismic recordings

¹³¹ and adjoint sources (Equation 15). We use a homogeneous elastic halfspace model (Table 1

¹³² True model) and use SPECFEM3D (Komatitsch & Tromp 2002) to simulate the synthetic

¹³³ seismic recordings. We set the model to be a 3km-length cube. We set the top surface of the

¹³⁴ cube to be a free surface and the other surfaces to be perfectly-matched layers. We discretize

¹³⁵ the whole cube into 30 m-length cubes. In one simulation, the time step is 0.0005 s and we

¹³⁶ propagate signals for 5000 time steps (i.e. 2.5 s). We simulate Z and R component data on

¹³⁷ the two receivers (r_A and r_B) due to 6720 vertical-point-force sources on the free surface

¹³⁸ (Figure 1a). Each source emits a 10 Hz Ricker wavelet with an amplitude factor of 10^{15} (F_z in

¹³⁹ Equation 5, also F_z^0 in Equation 15). Following Section 2.2, we do 4 simulations ($Z-$ and $R-$

¹⁴⁰ direction point forces at each receiver), and record at the 6720 seismic source locations. We

¹⁴¹ compute C_{ZZ} and C_{RR} (Equation 4). The phase of C_{ZZ} is identical to that of C_{RR} (Figure

¹⁴² 1b).

We focus on the sensitivity kernels for synthetic data in this section to study the kernel

structure. Therefore we simplify the misfit functions to

$$\chi(r_A, r_B) = T_{syn}, \tag{20}$$

$$\text{and } \chi(r_A, r_B) = \frac{1}{2} \int [w(t) C_{mn}(r_A, r_B, t)]^2 dt. \tag{21}$$

¹⁴³ These two simplified misfit functions indicate the traveltime and energy for main waveforms

¹⁴⁴ in crosscorrelations, respectively (Fichtner et al. 2017). The corresponding adjoint sources

Table 1. The homogeneous and isotropic elastic Earth model parameters used in the simulation.

Model	Vp (m/s)	Vs (m/s)	Density (kg/m^3)	Thickness (m)
True	2800	1500	2300	∞
Higher	3800	2000	2300	∞
Lower	1900	1000	2300	∞

145 are presented in Appendix A and B. The corresponding source kernels determine how source

146 strength changes affect the traveltime or waveform energy.

147 ### 3.1 Monochromatic source kernels

We now describe the monochromatic crosscorrelation source kernels from a physical point of view. In a homogeneous and isotropic media, under the far-field assumption, the vertical-component fundamental-mode Rayleigh-wave Greens function due to a vertical point force can be written as (e.g. Fan & Snieder 2009):

$$G_{ZZ}(r,\omega) = \sqrt{\frac{1}{8\pi\omega r/c}} e^{-i(\omega r/c + \pi/4)}, \tag{22}$$

where ω is the angular frequency, i is the imaginary unit, c is the surface-wave phase velocity and r is the distance between source and receiver. The negative sign in the exponential part of Equation 22 is due to the Fourier transform convention we use (Appendix D). If we consider a vertical-point-force seismic source on the free surface at r_s, the surface-wave crosscorrelation between two sensors (r_A and r_B) can be written as

$$C_{ZZ}(r_A, r_B, \omega, r_s) = \frac{1}{8\pi\omega/c} \sqrt{\frac{1}{r_{As}r_{Bs}}} e^{-i\omega(r_{As}-r_{Bs})/c}. \tag{23}$$

Following the same logic, and using

$$G_{RZ}(r,\omega) = \frac{H}{V} \sqrt{\frac{1}{8\pi\omega r/c}} e^{-i(\omega r/c - \pi/4)}, \tag{24}$$

where H/V is the ratio of the horizontal-to-vertical motion (e.g. Haney et al. 2012), we can write

$$C_{RR}(r_A, r_B, \omega, r_s) = \left(\frac{H}{V}\right)^2 \frac{1}{8\pi\omega/c} \sqrt{\frac{1}{r_{As}r_{Bs}}} cos(\theta_{As})cos(\theta_{Bs}) e^{-i\omega(r_{As}-r_{Bs})/c}, \tag{25}$$

where θ_{As} is the angle between the surface-wave propagation path and the radial direction (Figure 2). The phase of the Rayleigh wave is $\omega(r_{As} - r_{Bs})/c$ in Equation 23 and 25. These
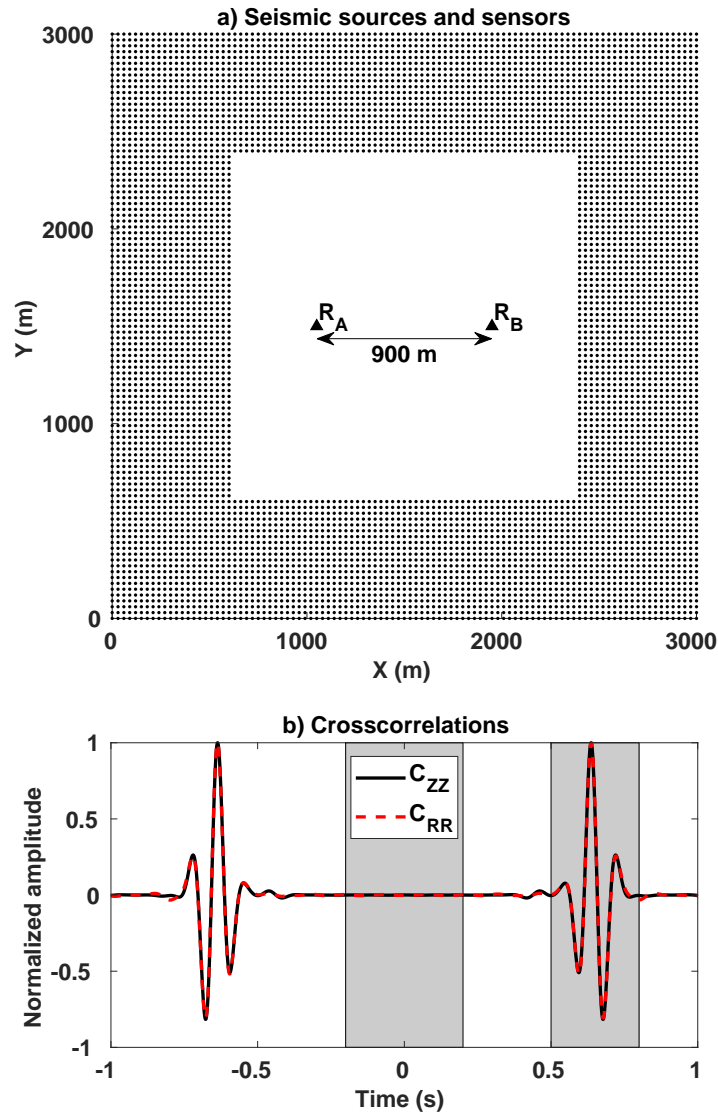
10   *Xu et al.*

Figure 1. a) Diagram of locations of the 6720 point sources and two receivers on the free surface. The black points represent point sources; the two black triangles represent the two receivers, r_A and r_B. b) The vertical-vertical (C_{ZZ}) and radial-radial (C_{RR}) crosscorrelation between the two receivers due to all sources in a). The two crosscorrelations are normalized by each maximum amplitude. The two gray blocks indicate two time windows, $-0.2 \sim 0.2$ and $0.5 \sim 0.8$ s.

phases remain constant if $r_{As} - r_{Bs}$ remains constant; $r_{As} - r_{Bs}$ will be constant if r_s is on a hyperbola with foci at r_A and r_B (Figure 2). Thus a certain phase corresponds to a hyperbola, comprised of r_s locations. For C_{ZZ} and C_{RR}, we focus on two specific phases:

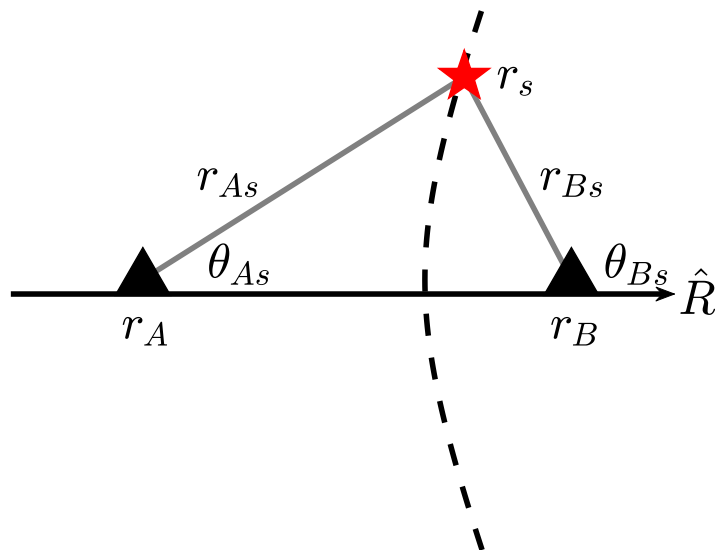$$-\frac{\omega(r_{As} - r_{Bs})}{c} = \phi_{obs} + 2N\pi, \tag{26}$$

Figure 2. Diagram of the location of a point source (star) and two sensors (triangles). The dashed hyperbola indicates potential source locations, where $r_{As} - r_{Bs}$ is constant. The radial direction, $\hat{R}$, is parallel to the line linking the two sensors, r_A and r_B.

and

$$-\frac{\omega(r_{As} - r_{Bs})}{c} = \phi_{obs} + (2N - 1)\pi, \tag{27}$$

where ϕ_{obs} is the phase of the observed waveform at frequency ω and $N = 0, \pm 1, \pm 2, \pm 3...$The two phases lead to two kinds of hyperbolas (Figure 3): $\phi_{obs} + 2N\pi$ phase leads to the same phase (ϕ_{obs}); the $\phi_{obs} + (2N - 1)\pi$ leads to the opposite phase ($\phi_{obs} \pm \pi$). These hyperbolas are determined by the value of ϕ_{obs}, which also change due with frequency (e.g. Xu et al. 2017).

These two kinds of crosscorrelations contribute ± 1 to the amplitude spectrum, but 0 to the phase spectrum of the Rayleigh waveform in C_{ZZ}. If we increase or decrease the source strength along one of these hyperbolas, the arrival time will not change because the corresponding phase spectrum does not change; however, the waveform energy will increase or decrease, respectively. This is because the sources along the hyperbola generate waveforms with exactly the same phase and arrival time. Therefore the hyperbola is located along the zero value in the traveltime kernels, and along the maximums and minimums of the waveform-energy kernels (Figure 3). Chmiel et al. (2018) observed similar source kernels with dense active-source seismic recordings and calculated the surface-wave phase velocities by fitting hyperbolas to the kernels using Equations 26 and 27.

We point out that the traveltime and waveform kernels for RR is stronger in the in-line areas than out-of-line areas (Figures 3b and 3d). This azimuthal effect is due to the $cos(\theta_{As})cos(\theta_{Bs})$ term in Equation 25. Xu & Mikesell (2017) observed this effect and noted
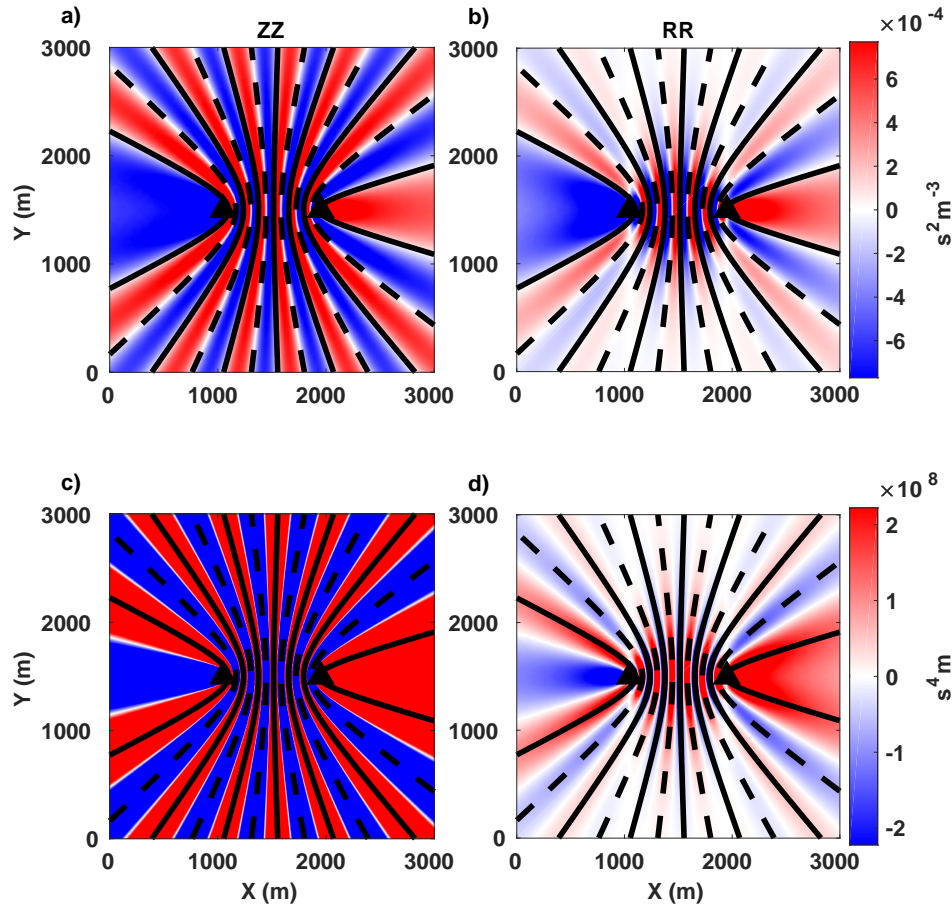
12   *Xu et al.*

Figure 3. Traveltime (top row) and waveform-energy (bottom row) source kernels computed at each grid node for 5 Hz direct Rayleigh waves in the causal parts of C_{ZZ} (left column) and C_{RR} (right column). The solid hyperbolas represent $2N\pi$ phase and the dashed represent $(2N-1)\pi$. The direct Rayleigh-wave time window is from 0.5 s to 0.8 s in Figure 1. These hyperbolas are asymmetric due to the value of ϕ_{obs} in Equations 26 and 27.

that this effect is frequency independent. The *cos* term can change sign with the receivers. Therefore the RR kernels can also change the sign of the kernel values, even if r_s moves along the same hyperbola as seen in Figure 3b and 3d. The absolute amplitude difference in the sensitivities between ZZ and RR kernels is due to the H/V ratio (Equation 25).

3.2   Multi-frequency source kernels

We stack the monochromatic source kernels over a frequency band, during which monochromatic kernels interfere with each other. In areas where these kernels share common sensitivity, the magnitude of sensitivity increases due to stacking. In other areas, the kernels destructively interfere and the magnitude decreases. Therefore, we observe that the direct Rayleigh waves
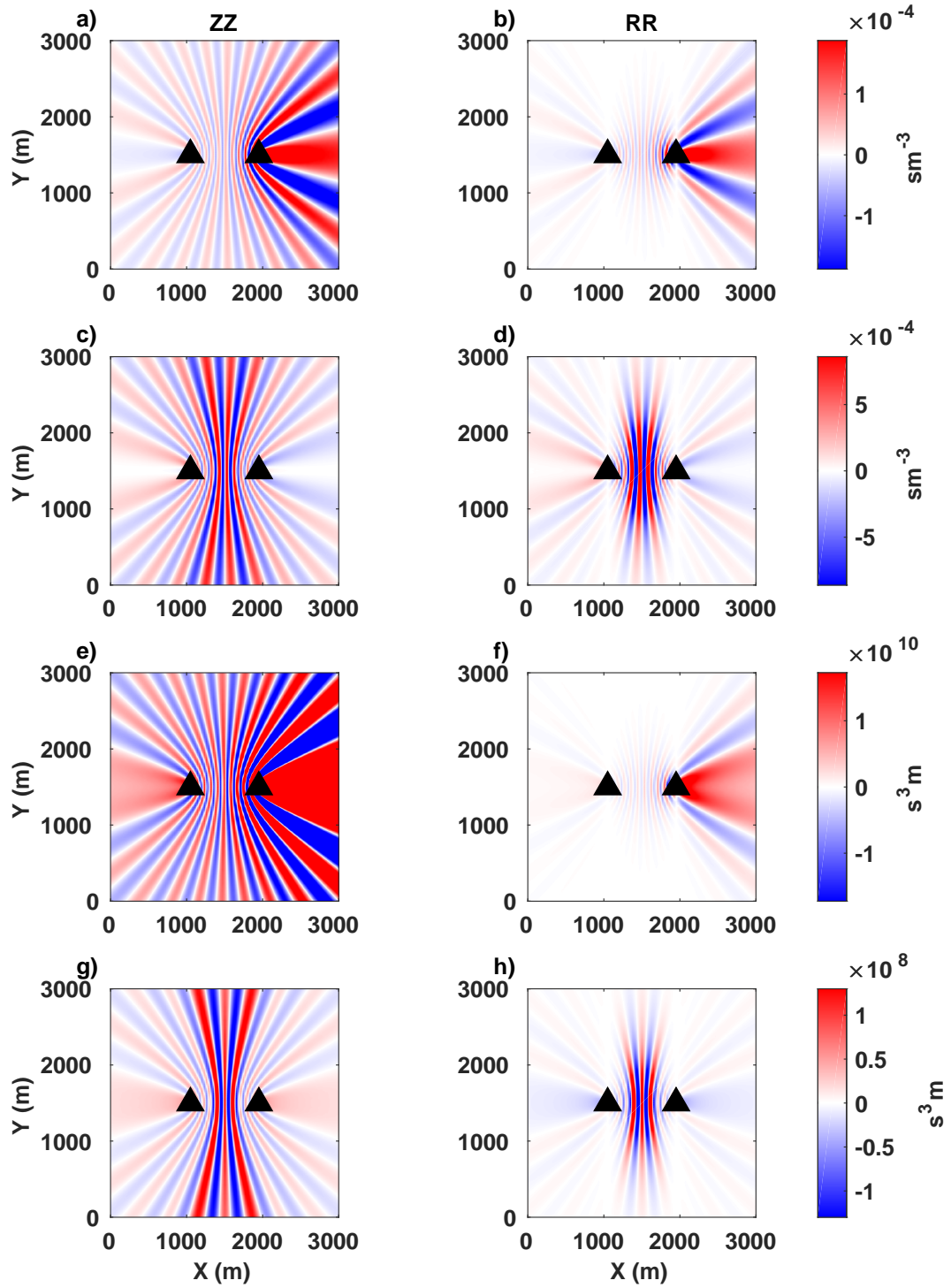
Figure 4. 2-8 Hz traveltime (a,b,c,d) and waveform-energy (e,f,g,h) source kernels for Rayleigh waves in C_{ZZ} (left) and C_{RR} (right). a,b,e,f are for direct Rayleigh waves (0.5 s to 0.8 s in Figure 1b); c,d,g and h are for early-arrival Rayleigh waves (-0.2 s to 0.2 s in Figure 1b).

14 *Xu et al.*

¹⁷⁴ in C_{ZZ} and C_{RR} are sensitive to sources in the in-line areas (Figure 4a, 4b, 4e, and 4f), the

¹⁷⁵ so-called stationary-phase zone (e.g. Snieder 2004). In this case we observe the majority of

¹⁷⁶ the sensitivity on the right-hand side of the model because we use a time window around

¹⁷⁷ the causal direct Rayleigh waves (Figure 1b). If we increase the in-line source strength, the

¹⁷⁸ traveltime and waveform energy will increase. This expectation fits the sensitivity sign in

¹⁷⁹ the in-line areas (Figure 4a, 4b, 4e, and 4f). For Rayleigh waves near the zero-time location

¹⁸⁰ (Figure 1b), we observe that both ZZ and RR taveltime and waveform-energy kernels are

¹⁸¹ sensitive to seismic sources between the two sensors (Figure 4c, 4d, 4g, and 4h).

¹⁸² We also observe the azimuthal effect in the RR kernels. Compared to the ZZ source

¹⁸³ kernels (Figure 4a, 4c, 4e, and 4g), the RR source kernels (Figure 4b, 4d, 4f, and 4h) possess

¹⁸⁴ less sensitivity to sources on the sidelobe areas. Thus for direct Rayleigh waves, we can use

¹⁸⁵ RR to focus on in-line seismic sources (Figure 4b and 4f) and decrease the error in Rayleigh-

¹⁸⁶ wave dispersion measurements due to anisotropic source distributions (e.g. van Wijk et al.

¹⁸⁷ 2011; Haney et al. 2012; Xu & Mikesell 2017). For Rayleigh waves near the zero point in

¹⁸⁸ crosscorrelations, where seismic sources occur between sensors, RR should help to locate the

¹⁸⁹ sources better than ZZ (Figure 4d and 4h vs 4c and 4g).

4 SOURCE ESTIMATION SYNTHETIC EXAMPLES

¹⁹¹ We present three synthetic source inversion examples to demonstrate that multicomponent

¹⁹² crosscorrelations (C_{RR} and C_{ZZ}) better estimate anisotropic source distributions than C_{ZZ}.

¹⁹³ We use 9 sensors in a square array in all examples. The smallest distance between two adjacent

¹⁹⁴ sensors is 450 m. We assume that all seismic sources are distributed on the free surface. In the

¹⁹⁵ first two examples, the seismic sources occur within the array area, with the sources distributed

¹⁹⁶ outside of the array in the third example. Each source emits a 10 Hz Ricker wavelet with an

¹⁹⁷ amplitude factor of 10^{15}. The subsurface is the same homogeneous media (Table 1 True model)

¹⁹⁸ as in Section 3. We assume that we know the subsurface structure and the source wavelet in

¹⁹⁹ the inversions. Thus we simulate the observed and synthetic crosscorrelations following Section

²⁰⁰ 3. We use the simulated wavefield to calculate the source kernels (Equation 15). We use both

²⁰¹ waveform and traveltime misfit functions (Equation 1 and 2), also C_{ZZ} and $C_{ZZ} + C_{RR}$ in the

²⁰² inversions. In using $C_{ZZ} + C_{RR}$ in misfit functions, we weight the two kinds of crosscorrelaions

²⁰³ equally by normalizing the amplitudes of C_{ZZ} and C_{RR} with the corresponding waveform

²⁰⁴ maximums in all sensor pairs.

²⁰⁵ We present the entire inversion algorithm as pseudocode (Algorithm 1). We adopt the

²⁰⁶ frequency band extension strategy (e.g. Virieux & Operto 2009). We use a large time window

Table 2. Traveltime and waveform inversion scheme details

	Traveltime	Waveform
Frequency band used in calculating misfit function and kernel	2-4/6/8/12/16 Hz	
Time window	0.6 s centered at the peak of crosscorrelation	-1 to 1 s
Crosscorrelation normalization term	Maximum in all C_{ZZ} or C_{RR}	
Smooth source strength per iteration	Yes	No
Update criteria, C_u	100%	99%
Stop criteria, C_s	0.01	0.01

in the waveform inversion (Table 2) because in the crosscorrelations the Rayleigh waves can arrive between time zero and the direct-wave arrival time, depending on the different source locations (e.g. Wapenaar & Fokkema 2006). This time-windowing strategy is in contrast to global earthquake seismology where we have accurate predictions of arrival times for body waves and Rayleigh waves (e.g. Maggi et al. 2009). If we use a narrow time window in the waveform inversion, artifacts appear outside the narrow time windows. However, the narrow time window works well for the traveltime inversion, because the traveltime inversion simply move waveforms forward or backward in time and thus no artifacts appear. We use the same frequency band to calculate the waveform source kernels and waveform misfit (Equation 1). We measure the traveltime misfits (Equation 2) over the whole frequency band because this measurement is more robust than in narrow frequency bands. We set the initial source strength at each sensor location to be zero. We smooth the source strength distributions in the traveltime inversions (see Algorithm 1), but not in the waveform inversions, because the traveltime source kernels possess narrower sensitivity bands than the waveform kernels (Figure 3 and 4). In practice, it is common to smooth the model parameters or gradients in wave-equation based tomography (e.g. Tape et al. 2007) and active-source waveform inversion (e.g. Groos et al. 2017). The inversion results are normalized by the maximum source strength, because we focus on relative source strength distributions, instead of absolute strength distributions.

16   *Xu et al.*

Algorithm 1 Inversion algorithm

  Normalize observed crosscorrelations by global maximums in C_{ZZ} and C_{RR};

  for ith iteration **do**

    forward source distribution model on N_i using Equation 4 and normalize crosscorrelations;

    calculate the misfit, χ_i, over time window using Equation 1 (waveform) or Equation 2 (traveltime);

    calculate adjoint source, f, using Equation B.3 (waveform) or Equation A.9 (traveltime);

    calculate the kernel, K, using Equation 15;

    for each step size, p_j **do**

      update N_i with p_j using Equation 19, (smoothing the updated source model with a 30 m 2D Gaussian filter in the traveltime inversion);

      forward model using source distribution and Equation 4;

      normalize crosscorrelations;

      calculate the misfit, χ_j;

    find the minimum misfit, $min(\chi_j)$, and the corresponding p_j ;

    if $min(\chi_j) < C_u\chi_i$ **then**

      update N_i and achieve N_{i+1} using Equation 19,(smoothing the updated source model with a 30 m 2D Gaussian filter in the traveltime inversion);

    else

      extend frequency band

    In the last frequency band

    if $|N_{i+1} - N_i|/|N_i| < C_s$ **then**

      stop inversion

4.1   Example 1: One source within array

The sensors surround one source area in this case (Figure 5a). The inversion results (Figure 5b, 5c, 5e, and 5f) estimate the source locations and strengths accurately, although the initial source distribution model (Figure 5d) is far from the true source model. We observe that the inverted source distribution from the waveform inversion (Figure 5e and 5f) are closer to the true source distribution than from the traveltime inversion (Figure 5b and 5c); the synthetic waveforms (Figure 5h) from the waveform inversion results also fit the observed C_{ZZ} better. This is because the waveforms contain not only traveltime information, but also information such as relative amplitudes. Thus, the waveform inversion performs better than
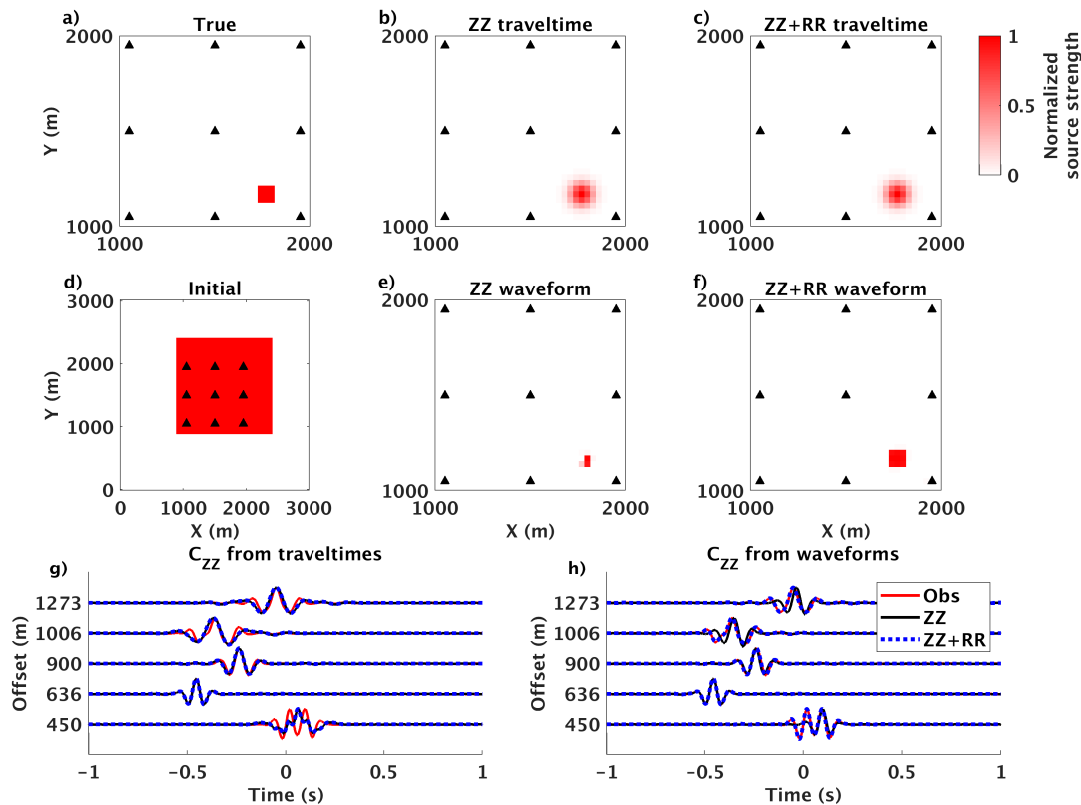
Figure 5. One source within array inversion results and the corresponding C_{ZZ} waveforms. a) The true source strength distribution is zeros everywhere except an in-array source area (square). Triangles are receivers. From the initial seismic source distribution model (d), we invert with the ZZ traveltimes (b), $ZZ + RR$ traveltimes (c), ZZ waveforms (e), and $ZZ + RR$ waveforms (f). We plot the synthetic C_{ZZ} based on the traveltime inversion results in (g) and the waveform inversion results in (h), along with the observed C_{ZZ}. Each waveform here is normalized by its maximum amplitude for comparison. Note that the initial source strength (d) at each receiver location is zero and is masked by the triangles.

234   the traveltime inversion. We note that the multicomponent data does not improve the source

235   distribution estimation when we only use traveltime information. The $ZZ + RR$ traveltime

236   inversion gives a similar source estimation to the ZZ inversion. However, multicomponent

237   data do help constrain the waveform inversion. In the waveform inversions, $ZZ + RR$ better

238   estimates the source shape than ZZ alone. Moreover, the synthetic C_{ZZ} waveforms from the

239   multicomponent inversion are closer to the waveforms of the observed C_{ZZ} (Figure 8g and h).
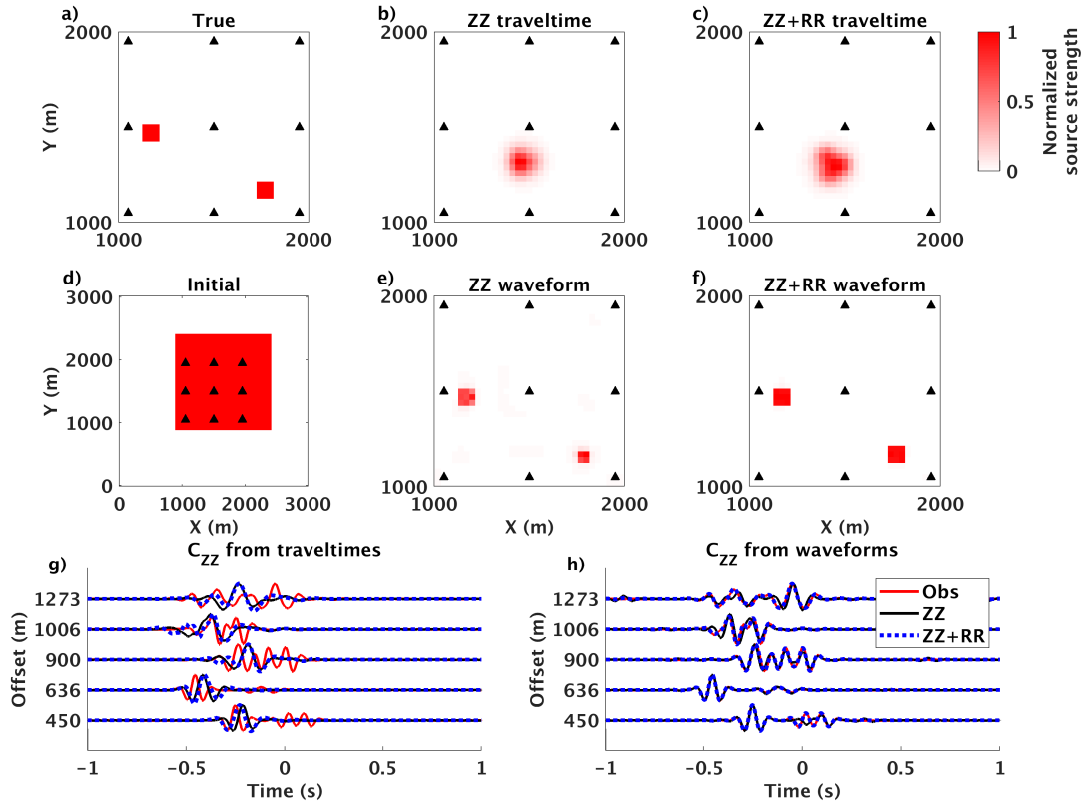
18   *Xu et al.*

Figure 6. Two sources within array inversion results and the corresponding waveforms. a) The true source strength is zeros everywhere except two source areas (squares) within the array (triangles). From the same initial source distribution model (d) as in Figure 5, we invert the ZZ traveltimes (b), $ZZ + RR$ traveltimes (c), ZZ waveforms (e), and $ZZ + RR$ waveforms (f). We plot the synthetic C_{ZZ} based on the traveltime inversion results in (g) and the waveform inversion results in (h), along with the observed C_{ZZ}. Each waveform here is normalized by its maximum amplitude for comparison. Note that the initial source strength (d) at each receiver location is zero and is masked by the triangles.

4.2   Example 2: Two sources within array

Two sources in the array make the observed crosscorrelation waveforms more complex than in the one-source case. We observe that more arrivals exist in the crosscorrelations from the two-source area (Figure 6h) than from one-source area (Figure 5h). We use the same initial source model as in the one-source case. The initial source strength model is far away form the true source model, so the corresponding synthetic waveforms are not similar to the observed waveforms. As the traveltime inversion mainly moves waveforms on the time axis, the synthetic waveforms from the traveltime inversion do not fit the observed data. For complex waveforms in the observed data (Figure 6g), where there are more than one arrival, we determine that
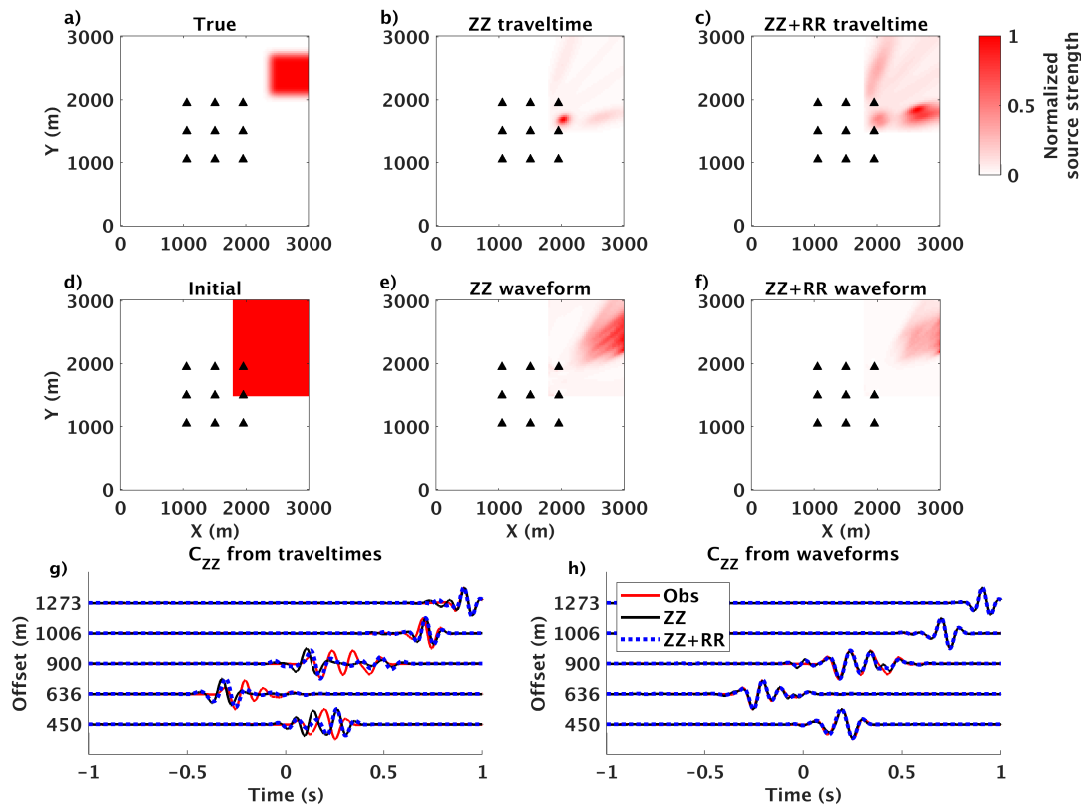
Figure 7. Source out-of-array inversion and the corresponding waveforms. a) The true source strength is zeros everywhere except the out-of-array source area (square). From an initial source model (d), we invert the ZZ traveltimes (b), $ZZ + RR$ traveltimes (c), ZZ waveforms (e), and $ZZ + RR$ waveforms (f). We plot the synthetic C_{ZZ} based on the traveltime inversion result in (g) and based on the waveform inversion result in (h), along with the observed C_{ZZ}. Each waveform here is normalized by its maximum amplitude for comparison.

249 the synthetic data from the traveltime inversions will not fit the observed data. Thus the

250 traveltime inversion gives incorrect, single-location estimations (Figure 6b and 6c). However,

251 the waveform inversion can handle the complex observed data because the waveform inversion

252 can fit multiple arrivals. We estimate accurate source locations and relative strengths with

253 the waveform inversion, and the synthetic C_{ZZ} from the inversion results fit the observed C_{ZZ}

254 well (Figure 6h). $ZZ + RR$ waveform inversion recovers the source shapes better than ZZ

255 waveform inversion.

20   *Xu et al.*

4.3   Example 3: Sources outside of array

Seismic sources lie outside of the array in this example. Thus neither method perfectly recovers the source shape as in the two previous examples (Figure 7). With the traveltime inversions, we determine that the inversion accurately provides an estimation of the directions of source locations, along with artifacts inside the array (Figure 7b and 7c), while the waveform inversion recovers the source location decently well (Figure 7e and 7f). Although the $ZZ+RR$ waveform inversion gives a similar result as the ZZ waveform inversion, the final misfit for $ZZ + RR$ is less than for ZZ (Figure 8f).

4.4   Analysis of inversion results

We observe that in the traveltime inversion examples, multicomponent data do not help to resolve the source distribution. In Example 1, $ZZ + RR$ gives a simiar misfit over the whole frequency band (2-16 Hz) as ZZ (Figure 8a). We ignore interpretation of Example 2 because the traveltime inversion does not work for this case as we explain in Section 4.2. When sources are outside of the array, $ZZ + RR$ gives a weaker artifact inside the array (Figure 7c) than does ZZ, but still neither traveltime inversion gives a correct result.

The multicomponent data improve the waveform inversion in all three examples. $ZZ + RR$ better estimates the source shapes for in-array sources and gives lower misfits than ZZ regardless of whether sources are in the array or not (Figure 8b, 8d and 8f). In Example 3, we observe that $ZZ + RR$ provides a similar estimation of seismic source distribution and a close misfit to ZZ (Figure 8f).

We also present seismic source estimation using matched-field processing (MFP) on the three examples (Figure C1). The MFP results recover true source locations, but also many artifacts. We demonstrate that MFP is equivalent to a waveform source kernel where the initial source strengths are zeros everywhere (Appendix C). These artifacts are suppressed by the waveform inversion and thus disappear in the inversion results (Figure 5e, 6e and 7e). One could use MFP results as an initial source model for the waveform inversion.

5   DISCUSSION

In calculating ambient seismic noise crosscorrelation functions, one usually adopt a stacking procedure to mitigate random uncorrelated noise (e.g. Bensen et al. 2007). Thus in real crosscorrelations, the main source of noise in crosscorrelations is due to correlated noise. We present noise-free examples in this paper to demonstrate the physics of the problem and the
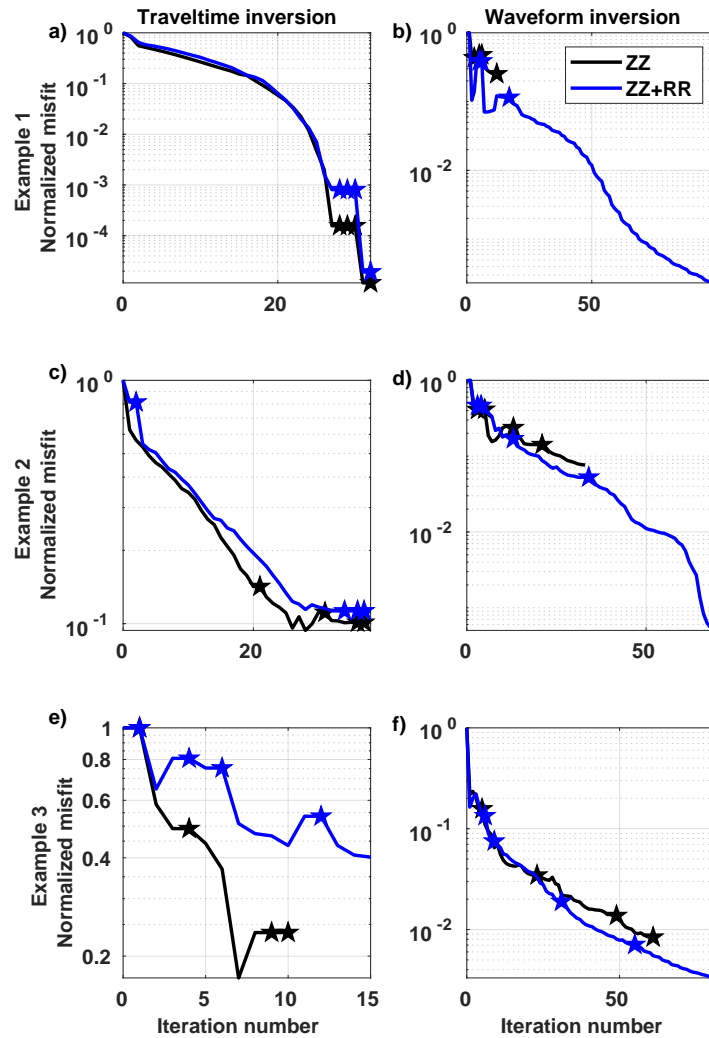
Figure 8. Traveltime and waveform inversion misfit comparisons. We show Example 1 (a and b), Example 2 (c and d), and Example 3 (e and f). The stars indicate when we extend the frequency bands (Table 2). We show the misfits over the whole frequency band, 2-16 Hz, relative to the initial misfit at each iteration.

properties of the adjoints. We address the topic of noise in our companion paper. For clarity here, we present three simple examples of one or two seismic sources within or outside of the array. The maximum number of sources we can estimate depends on the chosen misfit function (i.e. traveltime or waveform), the array geometry (i.e. the number of sensors and the inter-sensor distance), and the complexity of the sources (if sources cancel each other, e.g. Wapenaar & Fokkema 2006; Halliday & Curtis 2008). Further study of the topic of how many sources can one locate is beyond the scope of this research.

We make four assumptions in the crosscorrelation source distribution inversion procedure presented here:

22 *Xu et al.*

296 (i) seismic sources are only distributed on the free surface;

297 (ii) seismic sources are independent from each other;

298 (iii) the subsurface velocity model is known;

299 (iv) the source spectral shapes are similar and known.

300 We make the first assumption because we are concerned with only fundamental mode

301 Rayleigh waves (e.g. Halliday & Curtis 2008). Moreover, the ambient seismic noise > 2 Hz

302 is mainly due to human activity (e.g. Yamanaka et al. 1993) and composed of surface waves.

303 These seismic sources (e.g. traffic) usually occur on the surface or at shallow depths. We note

304 that could use the same theory and focus on body waves in the crosscorrelations to locate

305 seismic sources in depth. However, reverse-time migration is commonly used to locate the

306 microseismic sources (e.g. Artman et al. 2010). We present the link between the crosscorre-

307 lation source inversion and microseismic reverse-time migration in Appendix C. The second

308 assumption is often made in seismic interferometry (e.g. Weaver & Lobkis 2001). We discuss

309 the third assumption in this section, and a discussion of the fourth assumption is provided in

310 our companion paper, which considers field data.

311 Biased subsurface velocity models have been shown to lead to biased source locations

312 (e.g. Billings et al. 1994; Eisner et al. 2009). We use two incorrect velocity models (Table 1

313 Higher and Lower), where one has higher and the other has lower velocities than the true

314 velocity model. We use the same data, the same inversion strategies and the same initial

315 source models as in Section 4. We observe that we do not recover accurate source locations,

316 shapes of source areas, nor the number of source areas with the incorrect velocity models

317 (Figure 9 and 10). This phenomenon is expected because with these incorrect velocity models,

318 the crosscorrelations attribute the source to incorrect locations. For the same phase of a

319 crosscorrelation, $\omega(r_{As} - r_{Bs})/c$ in Equation 23, if we use an incorrect velocity, the $r_{As} - r_{Bs}$

320 will be larger or smaller than when using true velocity. Therefore the source inversion will

321 place sources at the wrong locations. For example, when sources are out of the array (Example

322 3), the waveform inversions give far away estimations of the source locations (Figure 9f and 9l)

323 with the higher-velocity model and closer estimations with the lower velocity model (Figure

324 10f and 10l).

325 We observe that the waveform inversion for all three synthetic data achieves the lowest

326 final misfit with the true velocity model, as does the traveltime inversion for one source within

327 the array (Figure 11). This observation indicates that one can potentially estimate the source

328 distribution and subsurface velocity structures through one inversion because the true source

329 distribution and true subsurface velocities give a global minimum in the misfit function (Figure

330 11a, 11d, 11e, and 11f). In practice, people estimate the source and velocity model iteratively

331 (e.g. Lee et al. 2014) or simultaneously (e.g. Sager et al. 2018). We also observe that the

332 multicomponent data, $ZZ + RR$, constrain the estimation better because the final normalized

333 waveform misfit for the true velocity model is the smallest and for the incorrect velocity model

334 is larger than ZZ.

6   CONCLUSION

336 We estimate the anisotropic source distribution of Rayleigh waves with vertical and multi-

337 component crosscorrelation inversion in this paper. We assume that we know the subsurface

338 structure. Through three synthetic examples, we show that multicomponent crosscorrelations

339 $(C_{ZZ} + C_{RR})$ do not help the traveltime inversion, but do help to resolve seismic source dis-

340 tributions more accurately than only the vertical crosscorrelations (C_{ZZ}) in the waveform

341 inversion. For the waveform inversion, both C_{ZZ} and $C_{ZZ} + C_{RR}$ provide accurate source

342 distributions for seismic sources within array, while $C_{ZZ} + C_{RR}$ estimate the source shapes

343 better. The $C_{ZZ} + C_{RR}$ waveform inversion gives a lower misfit than C_{ZZ} for sources within

344 and outside of the array. We also note that the crosscorrelation waveform inversion performs

345 better than the traveltime inversion. If the initial source model is far from the true source

346 distribution, the traveltime inversion can not fit the observed data, and thus gives biased

347 estimations. The waveform inversion is more robust to the initial source model because the

348 waveform inversion can fit complex observed waveforms with multiple arrivals. If sources are

349 outside of array, the traveltime and waveform estimate rough directions instead of exact source

350 shapes. Neither traveltime or waveform inversion works if the subsurface velocity model is in-

351 correct. However, for the waveform inversion and the in-array one-source traveltime inversion,

352 the true subsurface velocity model can give lower final misfit compared to incorrect velocity

353 models. $C_{ZZ} + C_{RR}$ makes the waveform misfit difference even larger than C_{ZZ}, and thus

354 better constrains estimation of the seismic source distribution and subsurface velocity model.

355 The source inversion we use in this paper not only handles seismic sources located at the free

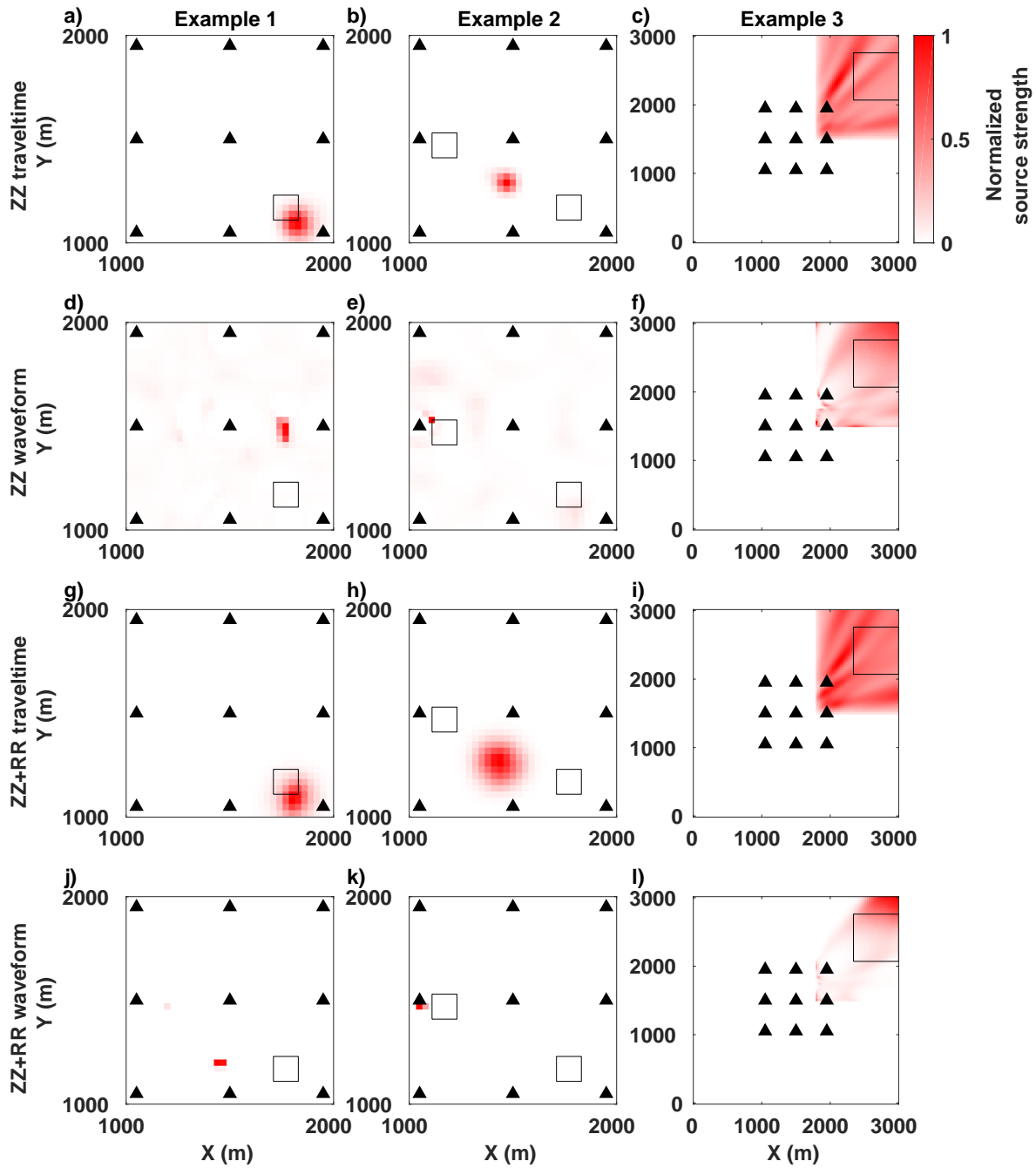356 surface, but also in depth.

7   ACKNOWLEDGEMENTS

24   *Xu et al.*

Figure 9. Source inversion results with a higher-velocity model (Table 1 higher). The black empty squares indicate the shapes and locations of the true sources. The initial models are as same as in Section 4.

363 **REFERENCES**

364 Aki, K. & Richards, P. G., 2002. *Quantitative Seismology*, Science Books.

365 Arai, H. & Tokimatsu, K., 2004. S-wave velocity profiling by inversion of microtremor H/V spectrum,
366 *Bulletin of the Seismological Society of America*, **94**(1), 53–63.

367 Ardhuin, F., Gualtieri, L., & Stutzmann, E., 2015. How ocean waves rock the Earth: Two mechanisms
368 explain microseisms with periods 3 to 300 s, *Geophysical Research Letters*, **42**(3), 765–772.

369 Artman, B., Podladtchikov, I., & Witten, B., 2010. Source location using time-reverse imaging,
370 *Geophysical Prospecting*, **58**(5), 861–873.

371 Aster, R. C., Borchers, B., & Thurber, C. H., 2011. *Parameter estimation and inverse problems*,
372 vol. 90, Academic Press.

373 Bensen, G. D., Ritzwoller, M. H., Barmin, M. P., Levshin, A. L., Lin, F., Moschetti, M. P., & Yang, Y.,
374 2007. Processing seismic ambient noise data to obtain reliable broad-band surface wave dispersion
375 measurements, *Geophysical Journal International*, **169**(3), 1239–1260.

376 Billings, S., Sambridge, M., & Kennett, B., 1994. Errors in hypocenter location: picking, model, and
377 magnitude dependence, *Bulletin of the Seismological Society of America*, **84**(6), 1978–1990.

378 Boaga, J., Cassiani, G., Strobbia, C. L., & Vignoli, G., 2013. Mode misidentification in Rayleigh
379 waves: Ellipticity as a cause and a cure, *Geophysics*, **78**(4), EN17–EN28.

380 Bozdağ, E., Trampert, J., & Tromp, J., 2011. Misfit functions for full waveform inversion based
381 on instantaneous phase and envelope measurements, *Geophysical Journal International*, **185**(2),
382 845–870.

383 Cheng, F., Xia, J., Luo, Y., Xu, Z., Wang, L., Shen, C., Liu, R., Pan, Y., Mi, B., & Hu, Y., 2016. Multi-
384 channel analysis of passive surface waves based on cross-correlations, *Geophysics*, **81**(5), EN57–
385 EN66.

386 Chmiel, M., Roux, P., Herrmann, P., Rondeleux, B., & Wathelet, M., 2018. Data-based diffraction
387 kernels for surface waves from convolution and correlation processes through active seismic interfer-
388 ometry, *Geophysical Journal International*, **214**(2), 1468–1480.

389 Corciulo, M., Roux, P., Campillo, M., Dubucq, D., & Kuperman, W., 2012. Multiscale matched-field
390 processing for noise-source localization in exploration geophysics, *Geophysics*, **77**(5), KS33–KS41.

391 Cros, E., Roux, P., Vandemeulebrouck, J., & Kedar, S., 2011. Locating hydrothermal acoustic sources
392 at Old Faithful Geyser using matched field processing, *Geophysical Journal International*, **187**(1),
393 385–393.

394 Dahlen, F., Hung, S.-H., & Nolet, G., 2000. Fréchet kernels for finite-frequency traveltimes-I. Theory,
395 *Geophysical Journal International*, **141**(1), 157–174.

396 Eisner, L., Duncan, P. M., Heigl, W. M., & Keller, W. R., 2009. Uncertainties in passive seismic
397 monitoring, *The Leading Edge*, **28**(6), 648–655.

398 Ermert, L., Sager, K., Afanasiev, M., Boehm, C., & Fichtner, A., 2017. Ambient seismic source inver-
399 sion in a heterogeneous Earth-Theory and application to the Earth's hum, *Journal of Geophysical*

26　　*Xu et al.*

Research: Solid Earth.

Fan, Y. & Snieder, R., 2009. Required source distribution for interferometry of waves and diffusive fields, *Geophysical Journal International*, **179**(2), 1232–1244.

Fichtner, A., 2015. Source-structure trade-offs in ambient noise correlations, *Geophysical Journal International*, **202**(1), 678–694.

Fichtner, A., Kennett, B. L., Igel, H., & Bunge, H.-P., 2008. Theoretical background for continental- and global-scale full-waveform inversion in the time–frequency domain, *Geophysical Journal International*, **175**(2), 665–685.

Fichtner, A., Stehly, L., Ermert, L., & Boehm, C., 2017. Generalised interferometry-I. Theory for inter-station correlations, *Geophysical Journal International*, **208**, 603–638.

Gribler, G., Liberty, L. M., Mikesell, T. D., & Michaels, P., 2016. Isolating retrograde and prograde Rayleigh-wave modes using a polarity mute, *Geophysics*, **81**(5), V379–V385.

Groos, L., Schäfer, M., Forbriger, T., & Bohlen, T., 2017. Application of a complete workflow for 2D elastic full-waveform inversion to recorded shallow-seismic Rayleigh waves, *Geophysics*, **82**(2), R109–R117.

Halliday, D. & Curtis, A., 2008. Seismic interferometry, surface waves and source distribution, *Geophysical Journal International*, **175**(3), 1067–1087.

Haney, M. M. & Nakahara, H., 2014. Surface-wave Greens tensors in the near field, *Bulletin of the Seismological Society of America*, **104**(3), 1578–1586.

Haney, M. M., Mikesell, T. D., van Wijk, K., & Nakahara, H., 2012. Extension of the spatial auto-correlation (SPAC) method to mixed-component correlations of surface waves, *Geophysical Journal International*, **191**(1), 189–206.

Harmon, N., Rychert, C., & Gerstoft, P., 2010. Distribution of noise sources for seismic interferometry, *Geophysical Journal International*, **183**(3), 1470–1484.

Ishii, M., Shearer, P. M., Houston, H., & Vidale, J. E., 2005. Extent, duration and speed of the 2004 Sumatra–Andaman earthquake imaged by the Hi-Net array, *Nature*, **435**(7044), 933.

Johansen, H., 1977. A man/computer interpretation system for resistivity soundings over a horizon-tally strafified earth, *Geophysical Prospecting*, **25**(4), 667–691.

Juretzek, C. & Hadziioannou, C., 2016. Where do ocean microseisms come from? A study of Love-to-Rayleigh wave ratios, *Journal of Geophysical Research: Solid Earth*, **121**(9), 6741–6756.

Komatitsch, D. & Tromp, J., 2002. Spectral-element simulations of global seismic wave propagation-I. Validation, *Geophysical Journal International*, **149**(2), 390–412.

Lee, E.-J., Chen, P., Jordan, T. H., Maechling, P. B., Denolle, M. A., & Beroza, G. C., 2014. Full-3-D tomography for crustal structure in southern California based on the scattering-integral and the adjoint-wavefield methods, *Journal of Geophysical Research: Solid Earth*, **119**(8), 6421–6451.

Liu, Q., Polet, J., Komatitsch, D., & Tromp, J., 2004. Spectral-element moment tensor inversions for earthquakes in southern California, *Bulletin of the Seismological Society of America*, **94**(5),

437   1748–1761.

438   Luo, Y. & Schuster, G. T., 1991. Wave-equation traveltime inversion, *Geophysics*, **56**(5), 645–653.

439   Maggi, A., Tape, C., Chen, M., Chao, D., & Tromp, J., 2009. An automated time-window selection

440   algorithm for seismic tomography, *Geophysical Journal International*, **178**(1), 257–281.

441   Nakata, N., Chang, J. P., Lawrence, J. F., & Boué, P., 2015. Body wave extraction and tomography at

442   Long Beach, California, with ambient-noise interferometry, *Journal of Geophysical Research: Solid*

443   *Earth*, **120**(2), 1159–1173.

444   Rayleigh, L., 1885. On waves propagated along the plane surface of an elastic solid, *Proceedings of*

445   *the London Mathematical Society*, **1**(1), 4–11.

446   Rhie, J. & Romanowicz, B., 2006. A study of the relation between ocean storms and the Earth's

447   hum, *Geochemistry, Geophysics, Geosystems*, **7**(10).

448   Rost, S. & Thomas, C., 2002. Array seismology: Methods and applications, *Reviews of geophysics*,

449   **40**(3).

450   Sager, K., Ermert, L., Boehm, C., & Fichtner, A., 2018. Towards Full Waveform Ambient Noise

451   Inversion, *Geophysical Journal International*, **212**(1), 566–590.

452   Shapiro, N. M., Michel, C., Laurent, S., & Ritzwoller, M. H., 2005. High-resolution surface-wave

453   tomography from ambient seismic noise, *Science*, **307**, 1615–1618.

454   Snieder, R., 2004. Extracting the Green's function from the correlation of coda waves: A derivation

455   based on stationary phase, *Physical Review E*, **69**(4), 046610.

456   Tape, C., Liu, Q., & Tromp, J., 2007. Finite-frequency tomography using adjoint methods–

457   Methodology and examples using membrane surface waves, *Geophysical Journal International*,

458   **168**(3), 1105–1129.

459   Thorson, J. R. & Claerbout, J. F., 1985. Velocity-stack and slant-stack stochastic inversion, *Geo-*

460   *physics*, **50**(12), 2727–2741.

461   Tian, Y. & Ritzwoller, M. H., 2015. Directionality of ambient noise on the Juan de Fuca plate:

462   Implications for source locations of the primary and secondary microseisms, *Geophysical Journal*

463   *International*, **201**(1), 429–443.

464   Traer, J. & Gerstoft, P., 2014. A unified theory of microseisms and hum, *Journal of Geophysical*

465   *Research: Solid Earth*, **119**(4), 3317–3339.

466   Tromp, J., Tape, C., & Liu, Q., 2005. Seismic tomography, adjoint methods, time reversal and

467   banana-doughnut kernels, *Geophysical Journal International*, **160**(1), 195–216.

468   Tromp, J., Luo, Y., Hanasoge, S., & Peter, D., 2010. Noise cross-correlation sensitivity kernels,

469   *Geophysical Journal International*, **183**(2), 791–819.

470   van Wijk, K., Mikesell, T. D., Schulte-Pelkum, V., & Stachnik, J., 2011. Estimating the Rayleigh-

471   wave impulse response between seismic stations with the cross terms of the Green tensor, *Geophysical*

472   *Research Letters*, **38**(16).

473   Virieux, J. & Operto, S., 2009. An overview of full-waveform inversion in exploration geophysics,

28   *Xu et al.*

474   *Geophysics*, **74**(6), WCC1–WCC26.

475   Wapenaar, K. & Fokkema, J., 2006.   Greens function representations for seismic interferometry,

476   *Geophysics*, **71**(4), SI33–SI46.

477   Weaver, R. L. & Lobkis, O. I., 2001. Ultrasonics without a source: Thermal fluctuation correlations

478   at MHz frequencies, *Physical Review Letters*, **87**(13), 134301.

479   Xu, Z. & Mikesell, T. D., 2017. On the reliability of direct rayleigh-wave estimation from multicom-

480   ponent cross-correlations, *Geophysical Journal International*, **210**(3), 1388–1393.

481   Xu, Z., Mikesell, T. D., Xia, J., & Cheng, F., 2017. A comprehensive comparison between the refraction

482   microtremor and seismic interferometry methods for phase-velocity estimation, *Geophysics*, **82**(6),

483   EN99–EN108.

484   Yamanaka, H., Dravinski, M., & Kagami, H., 1993. Continuous measurements of microtremors on

485   sediments and basement in Los Angeles, California, *Bulletin of the Seismological Society of America*,

486   **83**(5), 1595–1609.

487   Yang, Y. & Ritzwoller, M. H., 2008. Characteristics of ambient seismic noise as a source for surface

488   wave tomography, *Geochemistry Geophysics Geosystems*, **9**(2), 1256–1256.

489   Yao, H. & van Der Hilst, R. D., 2009. Analysis of ambient noise energy distribution and phase velocity

490   bias in ambient noise tomography, with application to SE Tibet, *Geophysical Journal International*,

491   **179**(2), 1113–1132.

492   **APPENDIX A: TRAVELTIME ADJOINT SOURCES**

We compute the perturbation of the traveltime misfit function (Equation 2) as:

$$\delta\chi = (T_{syn} - T_{obs})\delta(T_{syn} - T_{obs}) = (T_{syn} - T_{obs})\delta T, \tag{A.1}$$

where $T = T_{syn} - T_{obs}$ represents the travel-time difference between synthetic and observed waveforms. Fichtner et al. (2017) derived an expression for δT. We present the main steps here. The travel-time difference, T, is measured by crosscorrelation (Figure A1) and is determined as the crosscorrelation maximum (e.g. Luo & Schuster 1991; Dahlen et al. 2000):

$$T = max\left[\int C_{mn}(r_A, r_B, \tau)[w(\tau - t)C_{mn}^o(r_A, r_B, \tau - t)]d\tau\right], \tag{A.2}$$

where $w(t)$ is a time window and C_{mn}^o is the observed data. The time derivative of the max function argument at $t = T$ is zero. Thus we can write

$$\int C_{mn}(r_A, r_B, \tau)\frac{d}{dt}[w(\tau - t)C_{mn}^o(r_A, r_B, \tau - t)]_{t=T}d\tau = 0. \tag{A.3}$$

We then write the traveltime perturbation to T and C_{mn} as:

$$\int \delta C_{mn}(r_A, r_B, \tau) \frac{d}{dt}[w(\tau - t)C_{mn}^o(r_A, r_B, \tau - t)]_{t=T} d\tau$$

$$+ \int C_{mn}(r_A, r_B, \tau) \frac{d^2}{dt^2}[w(\tau - t)C_{mn}^o(r_A, r_B, \tau - t)]_{t=T} \delta T d\tau = 0, \qquad (A.4)$$

$$\rightarrow \delta T = -\frac{\int \delta C_{mn}(r_A, r_B, \tau) \frac{d}{dt}[w(\tau - t)C_{mn}^o(r_A, r_B, \tau - t)]_{t=T} d\tau}{\int C_{mn}(r_A, r_B, \tau) \frac{d^2}{dt^2}[w(\tau - t)C_{mn}^o(r_A, r_B, \tau - t)]_{t=T} d\tau}. \qquad (A.5)$$

One usually assumes that the observed waveform is a time-shifted copy of the synthetic waveform, $[w(\tau - t)C_{mn}^o(r_A, r_B, \tau - t)]_{t=T} = w(\tau)C_{mn}(r_A, r_B, \tau)$. In this case, we can rewrite the integrand of Equation A.5 as

$$\frac{d}{dt}[w(\tau - t)C_{mn}^o(r_A, r_B, \tau - t)]_{t=T} = -\frac{d}{d\tau}[w(\tau)C_{mn}(r_A, r_B, \tau)],$$

$$and \ \frac{d^2}{dt^2}[w(\tau - t)C_{mn}^o(r_A, r_B, \tau - t)]_{t=T} = \frac{d^2}{d\tau^2}[w(\tau)C_{mn}(r_A, r_B, \tau)].$$

Thus Equation A.5 becomes:

$$\delta T = \frac{\int \delta C_{mn}(r_A, r_B, \tau) \frac{d}{d\tau}[w(\tau)C_{mn}(r_A, r_B, \tau)] d\tau}{\int C_{mn}(r_A, r_B, \tau) \frac{d^2}{d\tau^2}[w(\tau)C_{mn}(r_A, r_B, \tau)] d\tau}, \qquad (A.6)$$

or in the frequency domain on a frequency band, $[\omega 1, \omega 2]$:

$$\delta T = i \frac{\int_{\omega 1}^{\omega 2} \omega \delta C_{mn}(r_A, r_B, \omega)[w(\omega) * C_{mn}(r_A, r_B, \omega)]^* d\omega}{\int_{\omega 1}^{\omega 2} \omega^2 C_{mn}(r_A, r_B, \omega)[w(\omega) * C_{mn}(r_A, r_B, \omega)]^* d\omega}. \qquad (A.7)$$

Finally, we write Equation A.7 with an adjoint source (f) for a single frequency (ω)

$$\delta T = \int_{\omega 1}^{\omega 2} f(\omega) \delta C_{mn}(r_A, r_B, \omega) d\omega. \qquad (A.8)$$

where

$$f(\omega) = i \frac{\omega[w(\omega) * C_{mn}(r_A, r_B, \omega)]^*}{\int_{\omega 1}^{\omega 2} \omega^2 C_{mn}(r_A, r_B, \omega)[w(\omega) * C_{mn}(r_A, r_B, \omega)]^* d\omega}. \qquad (A.9)$$

If we assume that we know the Green's functions (Equation 4), we can write

$$\delta T = \int_{\omega 1}^{\omega 2} \int_V G_{mp}(r_A, r_s, \omega) G_{np}^*(r_B, r_s, \omega) f(\omega) \delta S_p(r_s, \omega) dr_s d\omega, \qquad (A.10)$$

and we can write the source kernel for δT as

$$K_{mn}(\omega, r_s) = G_{mp}(r_A, r_s, \omega) G_{np}^*(r_B, r_s, \omega) f(\omega). \qquad (A.11)$$

493 Equation A.11 does not require observed data. Thus we use Equation A.11 in Section 3 to

494 analyze the traveltime source kernels. This formulation assumes that the observed waveform is

495 close to the synthetic waveform. As the assumption is not valid in our synthetic data examples,

496 we do not adopt Equation A.11 in the actual inversion algorithm.

30   *Xu et al.*

In the traveltime inversions (Section 4 and 5), we combine the kernel equation A.11 with Equation A.1 as:

$$
\begin{aligned}
K_{mn}^o(\omega, r_s) &= (T_{syn} - T_{obs})K_{mn}(\omega, r_s) \\
&= (T_{syn} - T_{obs})G_{mp}(r_A, r_s, \omega)G_{np}^*(r_B, r_s, \omega)f(\omega).
\end{aligned}
\tag{A.12}
$$

APPENDIX B: WAVEFORM ADJOINT SOURCES

We write the perturbation of the waveform misfit function (Equation 1) following Fichtner et al. (2017):

$$
\delta\chi = \int [w^2(t)(C_{mn}(r_A, r_B, t) - C_{mn}^o(r_A, r_B, t))]\delta C_{mn}(r_A, r_B, t)dt
\tag{B.1}
$$

$$
= \frac{1}{2\pi} \int [w(\omega) * w(\omega) * (C_{mn}(r_A, r_B, \omega) - C_{mn}^o(r_A, r_B, \omega))]^* \delta C_{mn}(r_A, r_B, \omega)d\omega,
\tag{B.2}
$$

where $\delta C_{mn}^o(r_A, r_B, \omega) = 0$. The corresponding adjoint source is defined as

$$
f(\omega) = \frac{1}{2\pi}[w(\omega) * w(\omega) * (C_{mn}(r_A, r_B, \omega) - C_{mn}^o(r_A, r_B, \omega))]^*.
\tag{B.3}
$$

In Section 3 where there is no observed crosscorrelation, we write the adjoint source as (Fichtner et al. 2017)

$$
f(\omega) = \frac{1}{2\pi}[w(\omega) * w(\omega) * C_{mn}(r_A, r_B, \omega)]^*.
\tag{B.4}
$$

APPENDIX C: THE LINK AMONG WAVEFORM SOURCE INVERSION, MATCHED-FIELD PROCESSING AND REVERSE-TIME MIGRATION

We can relate the waveform source inversion with the matched-field processing. If we assume that there are no seismic sources in the initial source distribution model, $C_{mn}(r_A, r_B, \omega)$ will be equal to zero. We can write the waveform source equation by combining Equation 9 and B.2 as

$$
\delta\chi = -\frac{1}{2\pi} \int \int_V [C_{mn}^o(r_A, r_B, \omega)]^* G_{mp}(r_A, r_s, \omega)G_{np}^*(r_B, r_s, \omega)\delta S_p(r_s, \omega)dr_s d\omega,
\tag{C.1}
$$

where we neglect the time window term $w(\omega)$. We then rewrite the observed crosscorrelation, $C_{mn}^o(r_A, r_B, \omega) = U_m^o(r_A, \omega)[U_n^o(r_B, \omega)]^*$, where $U_m^o(r_A, \omega)$ is the observed m-direction component seismic recording at r_A. The crosscorrelation at a single frequency is a component of the cross-spectral density matrix in matched-field processing (e.g. Cros et al. 2011). We now write the source kernel in Equation C.1 explicitly as

$$
K = -[U_m^o(r_A, \omega)]^* U_n^o(r_B, \omega)G_{mp}(r_A, r_s, \omega)G_{np}^*(r_B, r_s, \omega),
\tag{C.2}
$$

and rewrite Equation C.1 as

$$\delta\chi = -\frac{1}{2\pi}\int\int_V K\delta S_p(r_s,\omega)dr_s d\omega. \tag{C.3}$$

In practice, we stack the kernel among all sensor pairs and the stacked kernel reads as

$$K = -\sum_{r_A r_B}[U_m^o(r_A,\omega)]^*U_n^o(r_B,\omega)G_{mp}(r_A,r_s,\omega)G_{np}^*(r_B,r_s,\omega). \tag{C.4}$$

We can recognize the stacked kernel is a conjugation of the linear (Bartlett) processor in matched-field processing (e.g. Cros et al. 2011; Corciulo et al. 2012) without autocorrelation terms:

$$\sum_{r_A r_B}G_{zz}^*(r_A,r_s,\omega)U_z^o(r_A,\omega)[U_z^o(r_B,\omega)]^*G_{zz}(r_B,r_s,\omega), \tag{C.5}$$

500 where people usually use vertical component (Z) data. Therefore the matched-field processing
501 results are similar to the stacked waveform source kernels where the initial source strengths
502 are zero. We apply the matched-field processing to the ZZ data in Section 4 and estimate the
503 seismic source strengths shown in Figure C1. We calculate the Rayleigh-wave phase velocity
504 for the halfspace model (Table 1 True), 1391 m/s (Rayleigh 1885). We use Equation 22 as the
505 Green's function in MFP (Equation C.5) and estimate source distributions for each example
506 in Section 4 (Figure C1a, Figure C1b and Figure C1c). We observe that high source strength
507 values concentrate near the sensors and the true source locations. This singularity at the
508 sensors is due to the amplitude term in the Green's function, $\sqrt{\frac{1}{8\pi\omega r/c}}$. If we also only use
509 the phase part of the Green's function, the singularities disappear (Figure C1d, Figure C1e
510 and Figure C1f). The singularity also exists in the waveform inversion and that is why people
511 adopt a taper near sources and receivers or smooth the gradient (e.g. Groos et al. 2017).

We can also relate this kernel (Equation C.2) to reverse-time migration. If we assume that $C_{mn}^o(r_A,r_B,\omega)$ is due to a microseismic or secondary source, r', we can write the kernel as

$$K = [C_{mn}^o(r_A,r_B,\omega)]^*G_{mp}(r_A,r_s,\omega)G_{np}^*(r_B,r_s,\omega) \tag{C.6}$$

$$= [U_m^o(r_A,r',\omega)]^*U_n^o(r_B,r',\omega)G_{mp}(r_A,r_s,\omega)G_{np}^*(r_B,r_s,\omega) \tag{C.7}$$

$$= [U_m(r_A,r',\omega)G_{mp}^*(r_A,r_s,\omega)]^*[U_n(r_B,r',\omega)G_{np}^*(r_B,r_s,\omega)]. \tag{C.8}$$

512 We recognize that the kernel, Equation C.8, is the microseismic imaging condition (e.g. Art-
513 man et al. 2010, Equation 4) in the frequency domain. Therefore the imaging condition
514 in reverse-time migration is similar to the waveform source kernel with zero initial source
515 strength.

32 *Xu et al.*

APPENDIX D: FOURIER TRANSFORM CONVENTION

We use the following Fourier transform convention

$$U(\omega) = \int_{-\infty}^{\infty} U(t)e^{-i\omega t}dt, \tag{D.1}$$

as opposed to

$$U(\omega) = \int_{-\infty}^{\infty} U(t)e^{i\omega t}dt \tag{D.2}$$
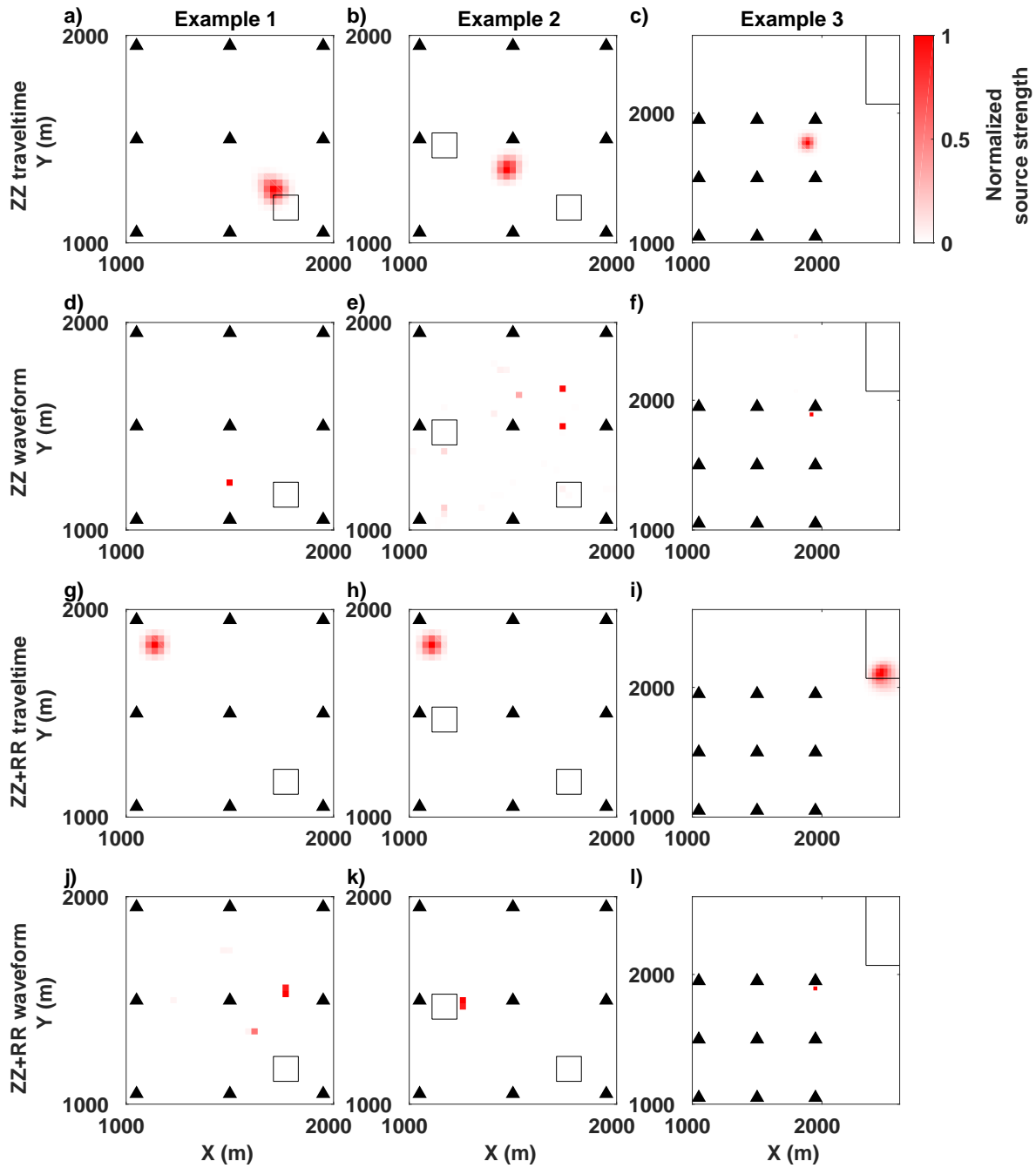
(e.g. Aki & Richards 2002; Haney & Nakahara 2014).

Figure 10. Source inversion results with a lower-velocity model (Table 1 lower). The black empty squares indicate the shapes and locations of the true sources. We only show the Example 3 results in a certain area because the source locations from the inversion are within this area. The initial models are as same as in Section 4.
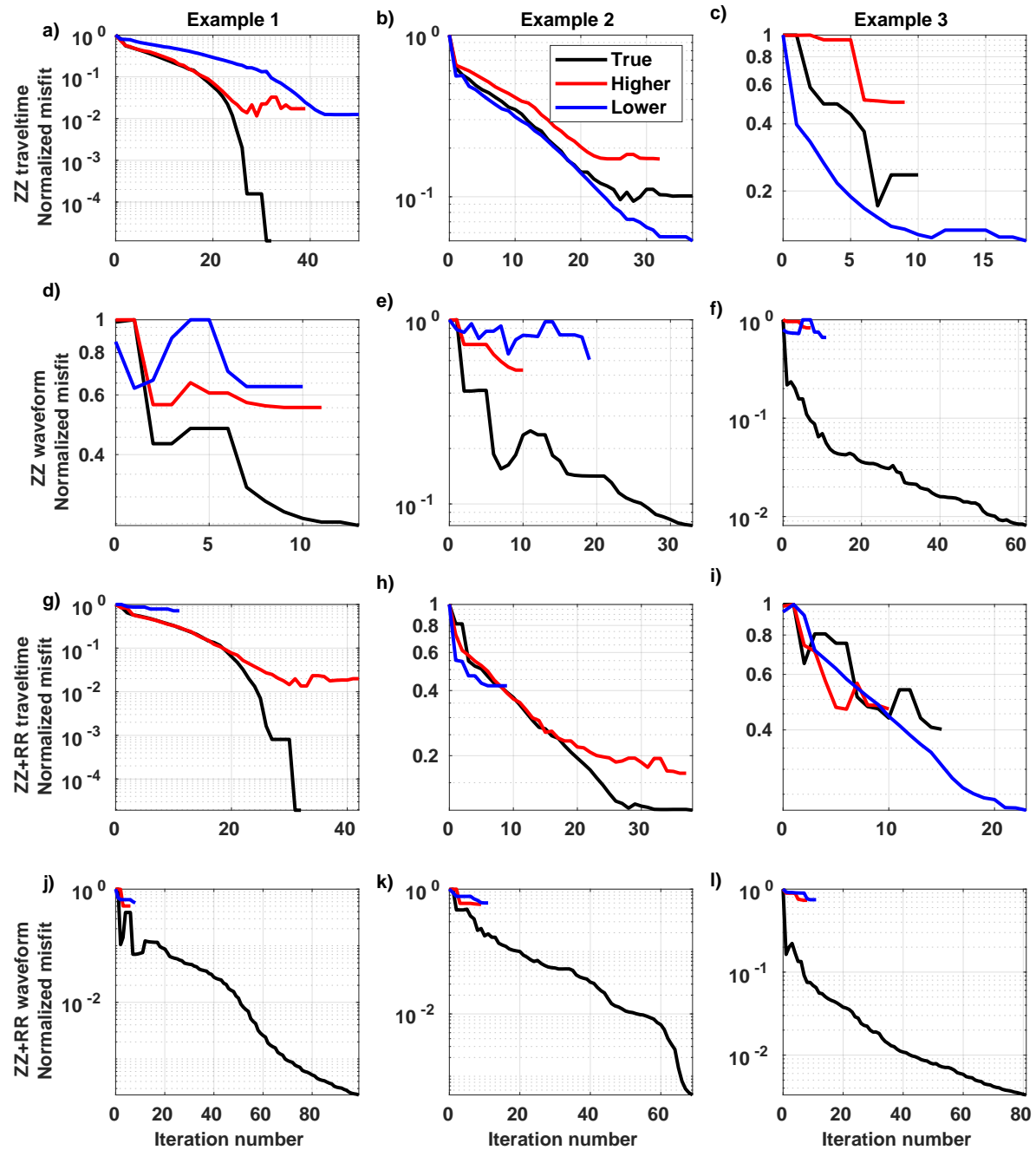
34   *Xu et al.*

Figure 11. Traveltime and waveform inversion misfit curves with true, higher and lower velocity models (Table 1).
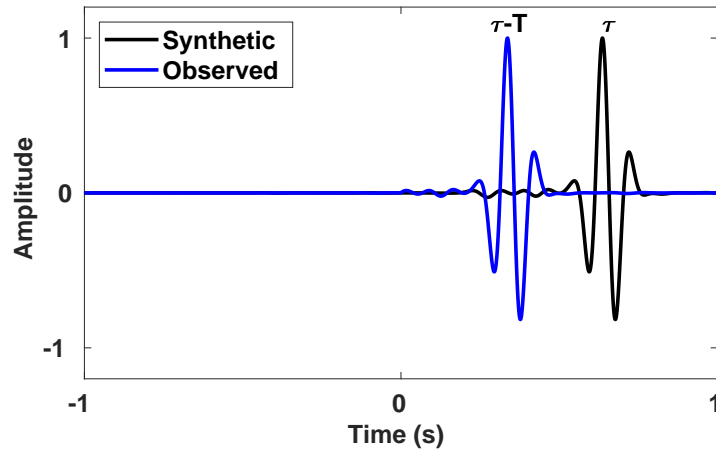
Figure A1. An illustration of the traveltime difference, T, between synthetic and observed crosscorrelations.
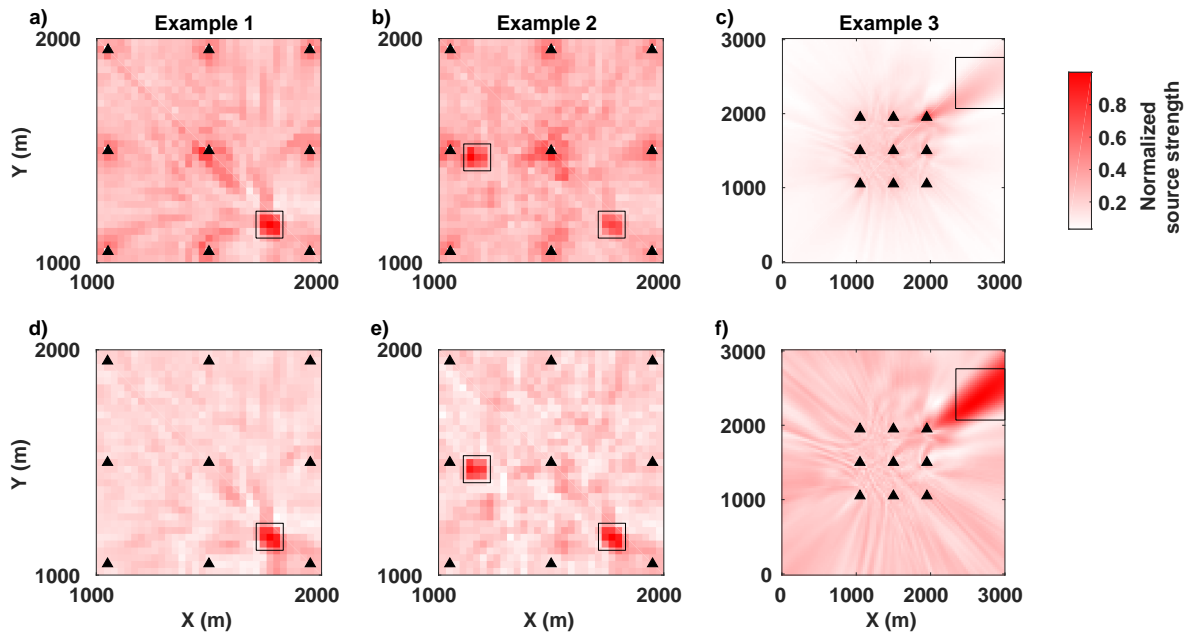

Figure C1. Matched-field processing (MFP) results from the ZZ data in Section 4. We use the full Rayleigh-wave Green's function (Equation 22) in MFP (a, b and c), and we only use the phase part of the Green's function (Equation 22) in MFP (d, e and f). The black empty squares indicate the shapes and locations of the true sources.